

Bhanja, A., Smythe, L., Herchel, R., Nemec, I., Murrie, M. and Ray, D. (2021) Hydroxido supported and differently networked octanuclear Ni_6Ln_2 [$\text{Ln} = \text{GdIII}$ and DyIII] complexes: structural variation, magnetic properties and theoretical insights. *Dalton Transactions*, 50(14), pp. 5023-5035. (doi: [10.1039/D0DT04168H](https://doi.org/10.1039/D0DT04168H))

There may be differences between this version and the published version. You are advised to consult the publisher's version if you wish to cite from it.

<http://eprints.gla.ac.uk/236386/>

Deposited on 11 March 2021

Enlighten – Research publications by members of the University of Glasgow
<http://eprints.gla.ac.uk>

Dalton Transactions

An international journal of inorganic chemistry

Accepted Manuscript

This article can be cited before page numbers have been issued, to do this please use: A. Bhanja, L. Smythe, R. Herchel, I. Nemec, M. Murrie and D. Ray, *Dalton Trans.*, 2021, DOI: 10.1039/D0DT04168H.



This is an Accepted Manuscript, which has been through the Royal Society of Chemistry peer review process and has been accepted for publication.

Accepted Manuscripts are published online shortly after acceptance, before technical editing, formatting and proof reading. Using this free service, authors can make their results available to the community, in citable form, before we publish the edited article. We will replace this Accepted Manuscript with the edited and formatted Advance Article as soon as it is available.

You can find more information about Accepted Manuscripts in the [Information for Authors](#).

Please note that technical editing may introduce minor changes to the text and/or graphics, which may alter content. The journal's standard [Terms & Conditions](#) and the [Ethical guidelines](#) still apply. In no event shall the Royal Society of Chemistry be held responsible for any errors or omissions in this Accepted Manuscript or any consequences arising from the use of any information it contains.

ARTICLE

Hydroxido Supported and Differently Networked Octanuclear Ni_6Ln_2 [$\text{Ln} = \text{Gd}^{\text{III}}$ and Dy^{III}] Complexes: Structural Variation, Magnetic Properties and Theoretical Insights

Received 00th January 20xx,
Accepted 00th January 20xx

DOI: 10.1039/x0xx00000x

Avik Bhanja,^a Lucy Smythe,^b Radovan Herchel,^c Ivan Nemec,^{c,d} Mark Murrie,^b Debashis Ray*,^a

The design and synthesis of Schiff base H_2L , (2-[[[2-hydroxy-3-methoxybenzyl]imino]methyl]phenol) bearing ONOO donor set has been explored for its reactivity pattern with $\text{LnCl}_3 \cdot 6\text{H}_2\text{O}$ ($\text{Ln} = \text{Gd}^{\text{III}}$ and Dy^{III}) and $\text{Ni}(\text{CH}_3\text{CO}_2)_2 \cdot 4\text{H}_2\text{O}$ in the presence of NEt_3 for molecular aggregation. Coordination driven spontaneous self-assembly reactions provides $[\text{Gd}_2\text{Ni}_6\text{L}_4(\mu_3\text{-OH})_6(\mu\text{-OH})_2(\text{CH}_3\text{CO}_2)_2(\mu\text{-H}_2\text{O})_2(\text{H}_2\text{O})_3(\text{MeOH})] \cdot 8\text{H}_2\text{O}$ (**1**), having 'butterfly-shaped' core and $[\text{Dy}_2\text{Ni}_6\text{L}_4(\mu_3\text{-OH})_4(\mu\text{-Cl})_2\text{Cl}_4(\text{H}_2\text{O})_2(\text{MeOH})_2] \cdot 2\text{MeOH} \cdot 4\text{H}_2\text{O}$ (**2**) with 'candy-shaped' core. Fusion of six partial cubane units led to mineral-like core in **1**, developed around central $\text{Ni}_2(\text{OH})_2$ moiety; whereas in case of **2**, four such partial cubanes are collapsed on $\text{Dy}_2(\text{OH})_2$. Direct-current (dc) magnetic susceptibility measurements reveal predominantly ferromagnetic interactions leading to a high-spin $S = 13$ ground state for **1**. Complex **2** exhibits slow relaxation of magnetization in a small applied dc field with an energy barrier to reorientation of the magnetization, $U_{\text{eff}} = 19.3$ K. The static and dynamic magnetic data are analysed and corroborated by density functional theory (DFT) and detailed CASSCF based calculations.

Introduction

In recent years synthetic endeavours toward the discovery of heteronuclear 3d–4f multimetallic coordination aggregates (MCAs), have attracted significant attention to rationalize the coordination behaviour of the designed ligand anions to manifest the unknown aggregation paths. Coordination networking of metal ions of two different types, having unique topology, often takes the supports of used organic ligands and account for their prospect to emerge as molecule-based magnets.^{1–2} These molecular magnets can exhibit slow relaxation of magnetization, can have applications in high-density information storage³, quantum computing^{4–5}, and molecular spintronics.^{6–7} Coordination aggregates with multiple metal centres often possesses high-spin ground state (S) with poor zero-field splitting (D). Incorporation of selected lanthanide ions within the MCA's with appreciable single ion magnetic anisotropy, is often associated with structural distortion and spin-orbit coupling,^{8–9} resulting increase of anisotropy barrier¹⁰ and suppression of ground state quantum tunneling of magnetization¹¹ (QTM), lead to slow relaxation of

magnetization.¹² High spin Ni^{II} ions have major contribution toward magnetic anisotropy¹³; moreover Ni^{II} ion also possesses ferromagnetic exchange interaction with the Ln^{III} ions.^{14–18} Widespread efforts can be exercise to synthesize new family of high nuclearity MCAs having aesthetically pleasing shapes like wheels, triangle, butterfly, stars etc. Appropriate functionalization on ligand backbone can provide two adjacent but different coordination sites suitable for coordination of both 3d and 4f ions. The Lewis acidic nature of hard trivalent 4f ions are suitable to initiate hydrolysis of bound H_2O molecules.¹⁹ Exploitation of such coordination induced hydrolytic reaction conditions around 4f ions, can result large numbers of hydroxido bridges, necessary for the growth of mineral-like magnetic cores.²⁰ Multinuclear hetero-metallic aggregates are well known during the last two decades, which includes e.g., Ni_8Ln_8 ²¹, Ni_5La_4 ¹³, $\text{Ni}_{12}\text{Gd}_{36}$ ²², $\text{Co}_{16}\text{Ln}_{24}$ ²³ and $\text{Cu}_{24}\text{Ln}_6$ ²⁴. Use of semi-rigid phenol-based Schiff base ligand system bearing flexible C–N and rigid –C=N sides is presumed to control the hydrolytic aggregation reaction following 3d ion bound initially formed fragments.²⁵

Herein, 2-[[[2-hydroxy-3-methoxybenzyl]imino]methyl]phenol (H_2L) (Fig. S1, ESI) was screened for preferential coordination of Ni^{II} and Gd^{III} / Dy^{III} ions. Systematic reaction protocol toward this endeavour resulted $[\text{Gd}_2\text{Ni}_6\text{L}_4(\mu_3\text{-OH})_6(\mu\text{-OH})_2(\text{CH}_3\text{CO}_2)_2(\mu\text{-H}_2\text{O})_2(\text{H}_2\text{O})_3(\text{MeOH})] \cdot 8\text{H}_2\text{O}$ (**1**) and $[\text{Dy}_2\text{Ni}_6\text{L}_4(\mu_3\text{-OH})_4(\mu\text{-Cl})_2\text{Cl}_4(\text{H}_2\text{O})_2(\text{MeOH})_2] \cdot 2\text{MeOH} \cdot 4\text{H}_2\text{O}$ (**2**) from the reactions of L^{2-} , $\text{Ni}(\text{CH}_3\text{CO}_2)_2 \cdot 4\text{H}_2\text{O}$ and $\text{GdCl}_3 \cdot 6\text{H}_2\text{O}$ or $\text{DyCl}_3 \cdot 6\text{H}_2\text{O}$, respectively. Two different 4f ions provided contrasting paths during the growth of octanuclear aggregates, is not usual in Ni–Ln family; encourage us to study the relevant functional behaviours in the solid state.

^a Department of Chemistry, Indian Institute of Technology, Kharagpur 721302, India

^b School of Chemistry, University of Glasgow, University Avenue, Glasgow G12 8QQ, U.K.

^c Department of Inorganic Chemistry, Faculty of Science, Palacky University, 17. listopadu 12, CZ-771 46 Olomouc, Czech Republic

^d Central European Institute of Technology, CEITEC BUT, Purkyňova 656/123, 61200 Brno, Czech Republic

†Electronic Supplementary Information (ESI) available: SHAPE analysis, Crystal data, PXRD curves, selected bond lengths and angles, TGA analysis, AC susceptibility and CASSCF calculations are described in Fig. S1–S14 and Tables S1–S8 in the text. CCDC 2021668 and 2021678 contain the supplementary crystallographic data for this paper. See DOI: 10.1039/x0xx00000x

Experimental Section

Reagents and Starting Materials

All the reactions performed for this work were done at room temperature in aerobic conditions. Solvents used in this work were purified²⁶ and all the starting materials used for this work were of reagent grade. 3-methoxysalicylamine was synthesized following a reported procedure.²⁷ The following chemicals were used as received without further purification: Ni(CH₃CO₂)₂·4H₂O, and NEt₃ (S. D. Fine Chemicals, Mumbai, India), DyCl₃·6H₂O and GdCl₃·6H₂O (Alfa Aesar, India), *o*-vanillin (Spectrochem Pvt. Ltd. Mumbai).

Synthesis of 2-[[2-hydroxy-3-methoxybenzyl)imino]methyl]phenol (H₂L)

The ligand H₂L was synthesized following our previously reported work.²⁸

Synthesis of 1–2

A general synthetic procedure was followed to obtain **1** and **2** in good yield. H₂L (0.025 g, 0.10 mmol) was dissolved in 10 mL of (2:1, v/v) MeOH–CHCl₃ solution. LnCl₃·6H₂O (0.05 mmol) (Ln = Gd³⁺ and Dy³⁺) and NEt₃ (0.02 g, 0.20 mmol) was added to the above solution and stirred for 2 h. Another 10 mL MeOH solution of Ni(CH₃CO₂)₂·4H₂O (0.025 g, 0.10 mmol) was then added and the green solution thus obtained was stirred for 3 h. To the filtered solution, 6 mL of CH₂Cl₂ was added and left undisturbed for slow evaporation. X-ray diffraction quality single crystals were isolated within 4–7 days and washed with cold EtOH.

[Gd₂Ni₆L₄(μ₃-OH)₆(μ-OH)₂(CH₃CO₂)₂(μ-H₂O)₂(H₂O)₃(MeOH)]·8H₂O (1). Yield: 0.036 g, 59% (based on Gd). Anal. Calcd for C₆₅H₉₅Gd₂Ni₆O₃₈ (2207.11): C, 35.37; H, 4.34; N, 2.54. Found: C, 35.12; H, 4.37; N, 2.51. Selected FT-IR data (KBr) cm⁻¹: 3369 (br), 1641 (m), 1595 (m), 1576 (m), 1475 (s), 1446 (m), 1409 (m), 1341(w), 1324(m), 1280 (s), 1222 (w), 1070 (s), 1034 (m), 853 (w), 745 (s), 600 (w).

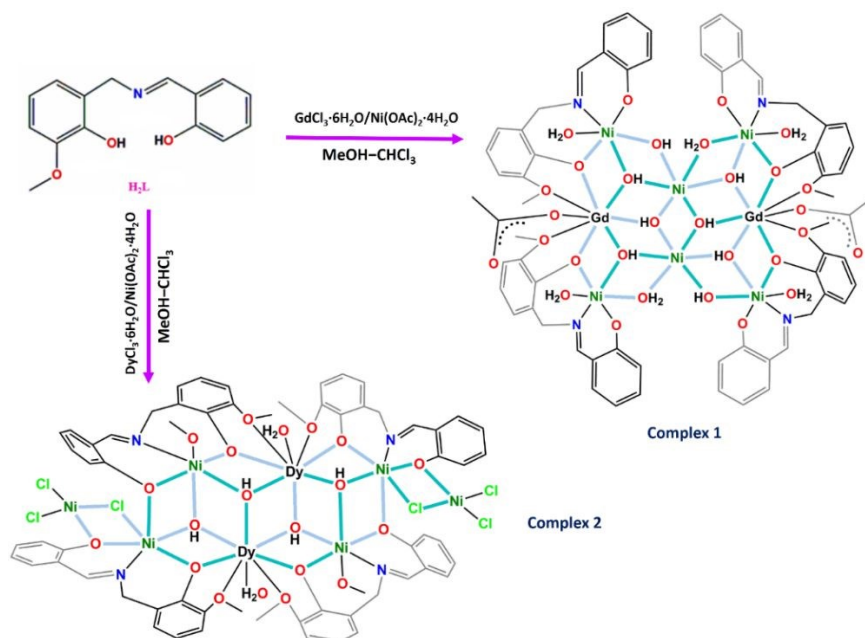
[Dy₂Ni₆L₄(μ₃-OH)₄(μ-Cl)₂Cl₄(H₂O)₂(MeOH)₂]·2MeOH·4H₂O (2). Yield: 0.029 g, 52% (based on Dy). Anal. Calcd for C₆₄H₈₄Cl₆Dy₂Ni₆O₂₆ (2215.24): C, 34.70; H, 3.82; N, 2.53. Found: C, 34.62; H, 3.79; N, 2.54. Selected FT-IR data (KBr) cm⁻¹: 1634 (m), 1550 (m), 1543 (m), 1476 (s), 1405 (m), 1287 (s), 1343 (w), 1227 (w), 851 (w), 737 (m), 602 (w).

Physical Measurements

Perkin-Elmer model RX1 FT-IR spectrometer was used to perform FT-IR spectral measurements using a KBr disk. For the Elemental analysis (C, H, N) of the complexes, a Perkin-Elmer model 240C elemental analyser was used. The purity of the bulk complexes were checked by powder XRD using a BRUKER AXS X-ray diffractometer (40 kV, 20 mA) using Cu-Kα radiation (λ = 1.5418 Å) within 5–50° (2θ) range and a fixed-time counting of 4 s at 25°C. Perkin Elmer Pyris Diamond TG-DTA instrument was used to perform thermogravimetric analysis.

Magnetic measurements

All magnetic measurements were carried out on powdered crystalline samples restrained in eicosane using a Quantum Design MPMS 3 SQUID magnetometer. Data were corrected for the diamagnetic contribution of the sample holder and eicosane by measurements, and for the diamagnetism of each compound.



Scheme 1 Synthetic Routes for **1** and **2**

X-ray Crystallography

Appropriate single crystals of **1** and **2** were chosen for data collection on a Bruker SMART APEX-II CCD X-ray diffractometer furnished with a graphite-monochromated Mo K α ($\lambda = 0.71073$ Å) radiation by the ω scan (width of 0.3° frame $^{-1}$) method at 112 K with a scan rate of 6 s per frame. SAINT and XPREP software's²⁹ were used for data processing and space group determination. The crystal structures were solved by direct method technique from SHELXS-2014³⁰ and then refined by full-matrix least squares technique using SHELXL (2014/7)³¹ program packaged within Olex-2.³² Empirical absorption correction was applied using the SADABS.³³ The locations of the heaviest atoms i.e. Ni, Gd or Dy were determined easily whereas the other non-hydrogen atoms were refined with anisotropic displacement parameters. The H atoms were incorporated at calculated positions and refined using the riding model. Crystallographic diagrams were presented using DIAMOND software.³⁴ Non-routine aspects of refinement: For both the complexes **1** and **2**, modelling of all lattice solvent molecules was not possible, due to disorder. So, mask program of Olex-2 software has been performed to remove those disordered solvent molecules and from the % weight loss of thermogravimetric analysis (Fig. S2, ESI), we have assigned 8H₂O for complex **1** and 2MeOH and 4H₂O for complex **2**, respectively. The disorder of the peripheral [NiCl₂] moiety in complex **2** has been improved by changing its occupancy which has been briefly discussed in the ESI. The crystal data and the cell parameters for compounds **1–2** are summarized in Table S1. Crystallographic data have been deposited with the Cambridge Crystallographic Data Centre as supplementary publications CCDC 2021668 and 2021678.

Theoretical calculations

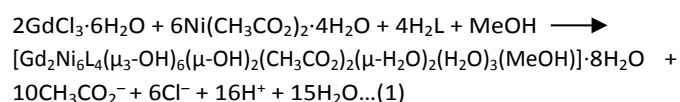
The theoretical calculations at DFT level were carried out with the ORCA 4.2 software^{35,36} and B3LYP hybrid functional.^{37–40} The DKH relativistic approximation^{41,42} with quadruple zeta basis SARC2-DKH-QZVP for Dy and SARC2-DKH-QZV for Lu,⁴³ DKH-def2-TZVP for Ni and DKH-def2-SVP for all other atoms.⁴⁴ The SARC/J Coulomb fitting basis set was utilized as an auxiliary basis set. Additionally, Gaussian finite nucleus model⁴⁵ was applied together with chain-of-spheres (RIJCOSX) approximation to exact exchange^{46,47} as implemented in ORCA. Increased integration grids (Grid7 and Gridx7 in ORCA convention) and tight SCF convergence criteria were used in all calculations. Moreover, the increased radial integration accuracy for Gd and Ni atoms was also set. The state average complete active space self-consistent field (SA-CASSCF)⁴⁸ wave functions calculations on Dy^{III} and Ni^{II} ions were done with OpenMOLCAS 19.11.⁴⁹ In the case of Dy^{III} ion, the active space was defined as 9 electrons in 7 f-orbitals, CAS(9,7). The RASSCF method was used in the CASSCF calculations with the following numbers of multiplets: 21 sextets, 224 quartets, and 490 doublets. In the case of Ni^{II} ions, CAS(8,5) active space was set resulting in 10 triplets and 15 singlets. The spin-orbit coupling based on atomic mean-field approximation (AMFI)^{50,51} was considered using RASSI-SO. While all multiplets of Ni^{II} were

included in this procedure, due to the large number of states of Dy^{III}, the number of states included in RASSI-SO was limited as follows: 21 sextets, 128 quartets, and 130 doublets. The relativistic effects were treated with the Douglas-Kroll Hamiltonian. The following basis sets were used: ANO-RCC-VQZP for Dy, ANO-RCC-VTZP for Ni and ANO-RCC-VDZP for coordinated oxygen/nitrogen atoms, while ANO-RCC-MB for all other atoms.^{52,52} After that SINGLE_ANISO module was applied to deduce the properties of paramagnetic ions. Subsequently, the home-made routine was used to fit experimental magnetic susceptibility in cooperation with POLY_ANISO module.^{54–56} All calculations were based on the experimental X-ray structures of **1** and **2**, in which only hydrogen atoms positions were modified with program Mercury using normalize hydrogen function.⁵⁷ The calculated spin density was visualized with VESTA 3 program.⁵⁸

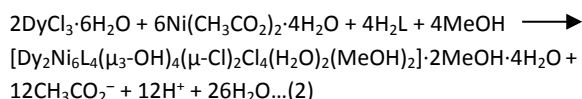
Results and Discussion

Design and synthesis

Schiff base H₂L has been synthesized from the reaction of *o*-vanillin amine and salicylaldehyde. Recently we have proved that this ligand H₂L having multiple numbers of donor atoms, is useful to provide Ni^{II}-Ln^{III} and Ni^{II}-Mn^{III}-Ln^{III} complexes while reacting with 3d metal ion salt along with Ln^{III} nitrate or Ln^{III} acetate salts.²⁸ Here we further explore its coordination potency in presence of Ln^{III} chloride and Ni^{II} metal ion salts in synergistic fashion. The stepwise reactions of H₂L with GdCl₃·6H₂O and NEt₃ in MeOH-CHCl₃ (2:1, v/v) solution followed by addition of Ni(CH₃CO₂)₂·4H₂O in 2:2:4:2 molar ratio provided [Gd₂Ni₆L₄(μ_3 -OH)₆(μ -OH)₂(CH₃CO₂)₂(μ -H₂O)₂(H₂O)₃(MeOH)]·8H₂O (**1**) (Scheme 1). The site selective coordination of different types of metal ion, followed by hydroxide bridge driven aggregation during the formation of **1**, summarized in the chemical eq. 1.



Liberation of in situ formed acetic acid, is in the line of typical reactivity of metal ion acetate with protonated ligand molecules, could guide the course of hydrolytic aggregation behaviour. The use of DyCl₃·6H₂O in place of GdCl₃·6H₂O resulted Ni₆Dy₂ aggregate of same number of individual 3d and 4f ions but interestingly of different molecular architecture. Varying path of hydrolytic aggregation and coordination of chloride ions to Ni^{II} centres resulted [Dy₂Ni₆L₄(μ_3 -OH)₄(μ -Cl)₂Cl₄(H₂O)₂(MeOH)₂]·2MeOH·4H₂O (**2**). Six available chlorido ligands from two DyCl₃·6H₂O are crucial in guiding a different route of aggregation for a diverse octanuclear 3d-4f complex resting on tetracubane core structure. The coordination aggregation reaction during synthesizing complex **2** is summarized in the chemical eq. 2.



Interestingly this type of reaction scheme with such lanthanide metal ion specificity is very rare in literature. The powder pattern of both the samples are matches well with simulated PXRD plot (Fig. S3 in the ESI). Initial characterization of the powder samples by FTIR spectral analysis indicated the metal ion binding through imine backbone of the ligand anion. For complex **1**, the $\tilde{\nu}_{\text{C=N}}$ stretching frequency lies at 1641 cm^{-1} whereas for complex **2** it is detected at 1634 cm^{-1} . The asymmetric and symmetric stretching frequency at 1595 cm^{-1} and 1324 cm^{-1} confirms the presence of terminal acetato ancillary group ($\Delta\tilde{\nu} = 271\text{ cm}^{-1}$) in complex **1**. We have tried our best, to extend our synthetic exploration for other Ln^{III} ions of similar size to explore further the role of 4f ions in variation of molecular structure, but unfortunately, we are not able to isolate any suitable single crystal from the attempted reactions using salts of other lanthanide ions.

Crystal Structure Description for Complex 1

Suitable single crystals of complex **1** were obtained after four days from the reaction mixture with added CH_2Cl_2 . The electro neutral complex crystallizes in triclinic $P\bar{1}$ space group. The asymmetric unit contains half of the whole molecule, where the ORTEP plots of same at 50% ellipsoid probability showed in Fig. S4 in the ESI. The molecular structure of complex **1** is then identified as $[\text{Gd}_2\text{Ni}_6\text{L}_4(\mu_3\text{-OH})_6(\mu\text{-OH})_2(\text{CH}_3\text{CO}_2)_2(\mu\text{-H}_2\text{O})_2(\text{H}_2\text{O})_3(\text{MeOH})] \cdot 8\text{H}_2\text{O}$ (Fig. 1). The crystal parameters are given in Table S1 and the selected bond length and angles are presented in Table S5–S6 in the ESI.

Examination of the molecular structure, indicates that four L^{2-} units are utilized for the growth of the molecular core bearing six Ni^{II} and two Gd^{III} ions. Four individual Ni^{II} ions directly bind to the imine pockets of four L^{2-} to yield four $\{\text{NiL}\}$ fragments having further coordination potential for Gd^{III} ions at the $-\text{OMe}_2\text{O}$ bi-dentate sites of the other available end. The participation of two such $\{\text{NiL}\}$ fragments coordinating with Gd^{III} ions helps to form this core. This core formed from six partial fused dicubane units with the participation of six $\mu_3\text{-OH}^-$, two $\mu\text{-OH}^-$ and two $\mu\text{-OH}_2$ units, which is rare in literature.²⁵ Within the $[\text{Ni}_6\text{Gd}_2\text{O}_{14}]^{6+}$ octanuclear core structure, the $[\text{Ni}_2(\text{HO})_2]^{2+}$ unit was trapped by two $[\text{Ni}_2\text{GdL}_2]$ parts with the association of several other HO^- bridges, forming the central $[\text{Ni}_2\text{Gd}_2\text{O}_6]^{4+}$ butterfly core⁵⁹, where the $[\text{Ni}_2(\text{OH})_2]^{2+}$ unit has no ligand anion support.

Complex **1** has distorted six-coordinate octahedral NO_5 and O_6 environments around three types of Ni^{II} centres ($\text{OC-6} = 0.544$ for Ni1 , 1.386 for Ni2 and 0.646 for Ni3 ; Table S2 in the ESI, Fig. 2). The imine nitrogen bound four NiNO_5 centres have one adjacent Ni^{II} and one Gd^{III} centres, bridged by $\mu_3\text{-HO}^-$ and PhO^- groups. On the contrary, two NiO_6 moieties are bridged by only hydroxido bridges. For the ligand coordinated Ni^{II} centres, the Ni-N distances of $1.989(7)$ – $1.997(8)\text{ \AA}$ range and

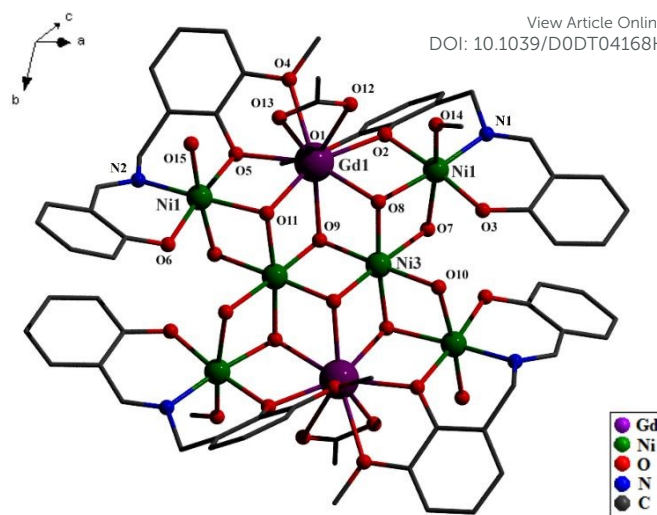


Fig. 1 Molecular view of **1** with partial atomic numbering scheme. H atoms and solvent molecules are omitted for clarity.

the Ni-O distances are in $1.982(6)$ – $2.201(6)\text{ \AA}$ range showing identifiable variation due to the presence of four different types of O donors. Interestingly the $\text{Ni-O}(\mu\text{-OH}_2)$ distances within $2.169(6)$ – $2.201(6)\text{ \AA}$ range are slightly longer than the $\text{Ni-O}(\mu\text{-OH})$ at $2.134(6)$ – $2.146(6)\text{ \AA}$, Ni-O from terminal H_2O at $2.089(6)$ – $2.111(7)\text{ \AA}$ and $\text{Ni-O}(\mu_3\text{-OH})$ at $2.018(6)$ – $2.077(6)\text{ \AA}$ distances, respectively. Out of the five $\text{Ni}\cdots\text{Ni}$ distances, three are unique; the $\text{Ni3}\cdots\text{Ni3}^*$ separation is $2.982(5)\text{ \AA}$ at the core. The $\text{Ni1}\cdots\text{Ni3}$ separation involving bridging HO^- and H_2O groups is longer at 3.164 \AA in comparison to 3.122 \AA for $\text{Ni2}\cdots\text{Ni3}^*$. The observed difference of 0.042 \AA is attributed to the weaker bridging potential of H_2O in comparison to HO^- .

The distorted nine-coordinate O_9 geometry around Gd1 and Gd1^* are assembled from two $-\text{OMe}_2\text{O}$ bites of L^{2-} , three HO^- bridges, and one bidentate terminal AcO^- group giving rise to a distorted muffin like arrangement as verified by SHAPE 2.1 calculations ($\text{MFF-9} = 2.087$, Table S3 in the Electronic Supporting Information, Fig. 3a). Four different Gd-O separations are observed within $2.32(6)$ – $2.69(2)\text{ \AA}$ range, following the order, $\text{Gd-O}_{\text{acetato}} > \text{Gd-O}_{\text{methoxido}} > \text{Gd-O}_{\text{hydroxido}} > \text{Gd-O}_{\text{phenoxido}}$. Within the central Ni_2Gd_2 partial dicubane part the $\text{Ni3}\cdots\text{Gd1}$, $\text{Ni3}\cdots\text{Gd1}^*$ and $\text{Gd1}\cdots\text{Gd1}^*$ distances are longer at $3.453(5)\text{ \AA}$, $3.471(4)\text{ \AA}$ and $6.249(7)\text{ \AA}$ respectively. Here, the Ni-O and Gd-O distances lie within $2.018(6)$ – $2.064(5)\text{ \AA}$ and $2.382(7)$ – $2.389(6)\text{ \AA}$ respectively. The bond angles around $\mu_3\text{-OH}^-$ are, $\angle\text{Ni3-O9-Gd1} = 101.9(19)^\circ$, $\angle\text{Ni3}^*\text{-O9-Gd1} = 102.1(19)^\circ$ and for $\angle\text{Ni3-O9-Ni3}^* = 92.8(2)^\circ$ showing the flattened cube vertex at the bigger Gd^{III} ions (Fig. 3b). The other Ni-O-Gd angles are also wider, $\angle\text{Ni3-O8-Gd1}$; $103.1(2)^\circ$ and $\angle\text{Ni3}^*\text{-O11-Gd1}$; $103.5(2)^\circ$. The Ni-O-Ni angle is slightly narrow for aqua bridged structure $\angle\text{Ni1-O7-Ni3}$; $92.8(2)^\circ$ compared to $\angle\text{Ni2-O10-Ni3}$ of $93.7(2)^\circ$ for hydroxide bridging. All the six Ni^{II} centres remain within the plane and the Gd1 and Gd1^* atoms show deviation by 0.253 \AA from the

plane. No characteristic non-covalent and intermolecular interactions

View Article Online
DOI: 10.1039/D0DT04168H

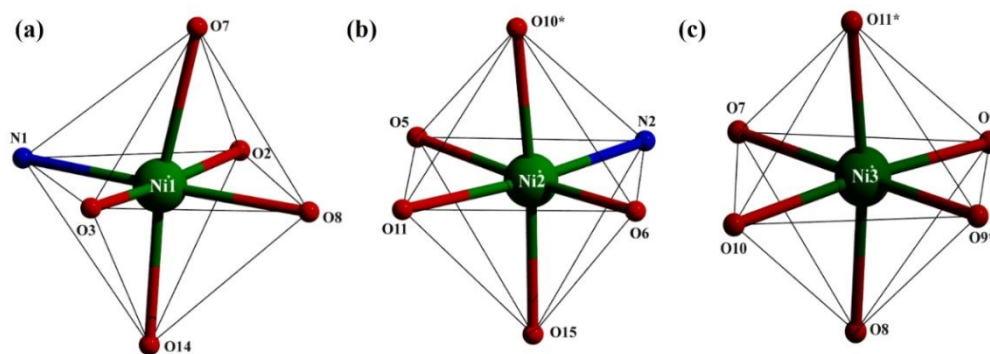


Fig. 2 Three types of Ni^{II} centre geometry present in complex 1: (a) Ni1/Ni1* (b) Ni2/Ni2* and (c) Ni3/Ni3*.

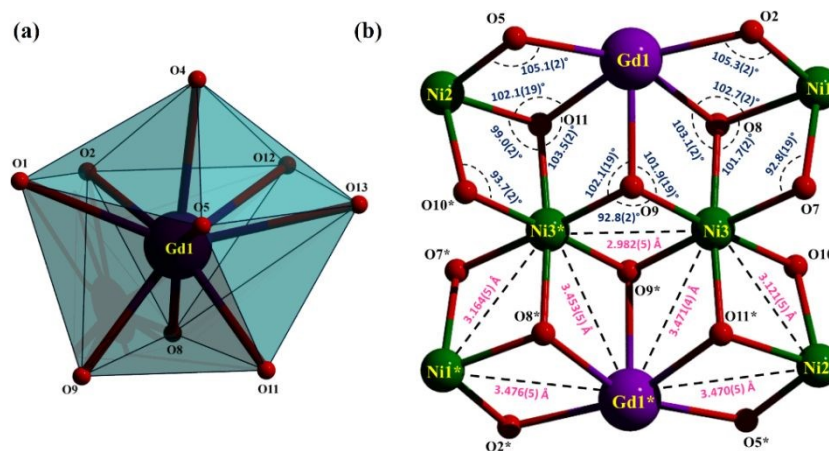


Fig. 3 (a) Distorted muffin coordination geometry around the Gd^{III} centres; (b) Core view of 1 with intermetallic distances and important angles within the fused hexacubane core.

are observed, except two weak hydrogen bonding interactions between the coordinated H₂O and dangling O atoms of adjacent acetate groups.

Crystal Structure Description for Complex 2

Needle-shaped single crystals of **2** were obtained after one week from the reaction mixture following solvent evaporation. The neutral complex [Dy₂Ni₆L₄(μ₃-OH)₄(μ-Cl)₂Cl₄(H₂O)₂(MeOH)₂·2MeOH·4H₂O crystallizes in monoclinic space group C2/c (Fig. 4). The ORTEP plots of asymmetric unit viz., [Ni₃DyL₂(μ-OH)₂(μ-Cl)Cl₂(H₂O)(MeOH)] with 50% ellipsoid probability showed in Fig. S5 of ESI. The crystal parameters of **2** are given in Table S1 and the selected bond length and angles are in Table S7–S8 in the ESI.

The analysis of molecular structure revealed that each L²⁻ unit binds single Ni^{II} centre through its imine N and adjacent O donors to yield {NiL} fragments suitable to trap oxophilic Dy^{III} ions through free -OMe donor and bridging action of O donor of already bound phenolate group. Two such {NiL} fragments in opposite directions bind a single Dy^{III} ion to afford {Ni₂DyL₂} units susceptible for aggregation. Fusion of four partial open cubes *via* four solvent derived μ₃-OH and six μ-Oph bridges from L²⁻ finally results the Ni₆Dy₂ complex **2**. The six-

coordinated Ni^{II} centres are of two types in distorted octahedral NO₅ or NO₄Cl environments (OC–6 = 0.937 for Ni1 and 1.386 for Ni2, Table S2 in the ESI) and the tetrahedral four coordinated sites are completed within Cl₃O milieu (Fig. 5). The τ₄ index⁶⁰ for slight D_{2d} distortion around the Ni3/Ni3* centres is found to be 0.997 (τ₄ is 0 and 1 for perfect square planar and tetrahedral geometries, respectively). The in-situ generated NiCl₂ parts link terminal chlorido and bridging phenoxido groups with Ni2 and Ni2* to stabilize the tetrahedral sites. Longer N1–Ni1, 2.011(7) Å and O7–Ni1, 2.132(5) Å bonds

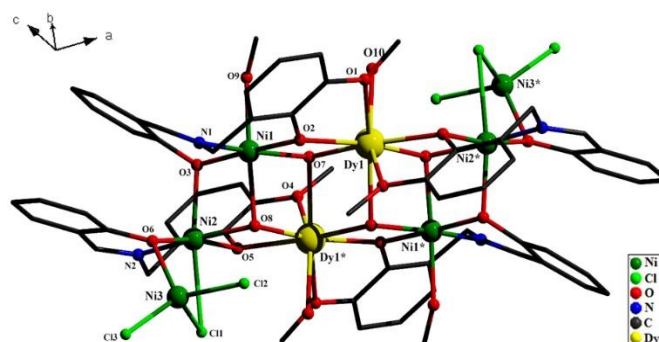


Fig. 4 Molecular structure of complex 2 with partial atomic numbering scheme. H atoms and solvent molecules were omitted for clarity.

result longest N1–Ni1–O7 axis around Ni1(Ni1*). Similarly, for Ni2/Ni2* the longest alignment is Cl1–Ni2–O3 from longer Cl1–Ni2, 2.658(3) Å and O3–Ni2, 2.078(6) Å bonds. Around tetrahedral Ni^{II} centres (Ni3/Ni3*), the Cl–Ni3 bond distances vary within 2.188(3)–2.320(3) Å range. Presence of three different types of O donors lead to appreciable modulation in the Ni–O bond distances from 1.971(6) Å to 2.132(5) Å. Three diverse types of Ni^{II} centres are responsible for registering Ni1...Ni2 and Ni2...Ni3 separations of 3.079(12) Å and 3.110(12) Å, respectively. The Ni–O–Ni angles at the phenoxido and hydroxido heads are different at 97.4(2)° (∠Ni1–O3–Ni2), 102.2(2)° (∠Ni2–O6–Ni3) and 96.3(19)° (∠Ni1–O8–Ni2). The Ni2–Cl1–Ni3 angle is acute enough at 77.1(18)° due to the presence of longer Ni2–Cl1 bond at 2.658(3) Å.

Bigger Dy1 and Dy1* centres in O₈ coordination environment is accomplished by bidentate –OMe₂O parts of L^{2–}, three HO[–] bridges, and one terminal H₂O donor. Placement of eight oxygen donors around Dy1 and Dy1* centres reveal distorted trigonal dodecahedron environments supported by SHAPE 2.1 (TDD-8 = 0.835 in Table S4 in the ESI, Fig. 6a). Unlike complex **1**, here Dy1 and Dy1* are bridged by two μ₃-HO[–] groups to form a Dy₂O₂ rhombus having ∠Dy1–O7–Dy1* and ∠O7–Dy1–O7* angles of 106.4(19)° and 73.6(18)° respectively providing the Dy1...Dy1* separation of 3.743(14) Å (Fig. 6b).

Four different types of oxygen donors, around the each Dy^{III} centre resulted variation in Dy–O bond distances from 2.263(5) Å to 2.532(6) Å, where the longest one is registered for –OMe function as Dy1–O4. The Ni–O–Dy angles at different bridges register angles from 100.5(2)° to 107.2(2)° and the Ni...Dy remain within 3.408(13)–3.463(13) Å range. The μ-phenoxido bridges are wider at 105.2(2)°–107.3(2)° compared to μ₃-hydroxido bridges within 101.0(2)°–102.1(2)°. All the metal ion centres in the central Ni₄Dy₂ unit are mostly coplanar, and the Ni3 and Ni3* centres are 3.185 Å away from the best plane.

Magnetic Studies

The temperature dependent magnetic susceptibility values of complexes **1** and **2** were measured from 2–290 K in a field of 0.1 T and the χT versus T data are shown in Fig. 7. At 290 K, χT = 23.6 cm³ mol^{–1} K for complex **1**, and 35.3 cm³ mol^{–1} K for complex **2**, which are consistent with the expected values for these complexes at room temperature (χT_{calc} = 22.7 cm³ mol^{–1} K for **1** { g_{Ni} = 2.15 and g_{Dy} = 2.0} and 35.3 cm³ mol^{–1} K for **2** { g_{Ni} = 2.15 and g_{Dy} = 4/3}). As the temperature decreases, the χT value for complex **1** increases to 74.2 cm³ mol^{–1} K at 3 K, before decreasing slightly to 73.0 cm³ mol^{–1} K at 2 K. The χT vs. T data for complex **1** is consistent with a large spin ground state resulting from predominantly ferromagnetic intra-molecular exchange interactions and the presence of zero-field

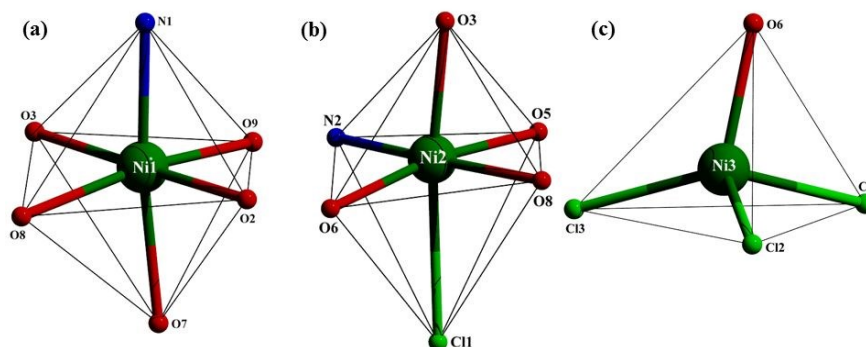


Fig. 5 Ni^{II} centres in complex **2**: (a) distorted octahedral geometry in Ni1/Ni1* and (b) Ni2/Ni2* (c) slightly distorted tetrahedral geometry in Ni3/Ni3*.

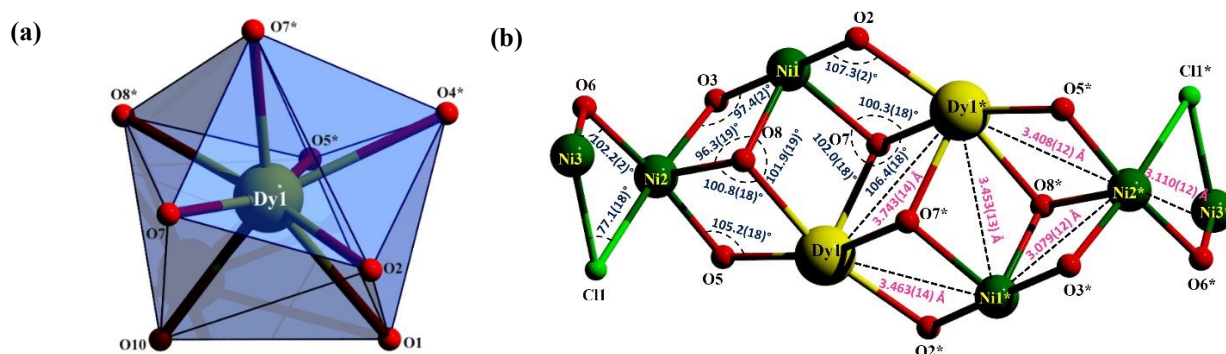


Fig. 6 (a) Distorted trigonal dodecahedral coordination geometry around the two Dy^{III} centres; (b) Core view of **2** with intermetallic distances and angles.

splitting (ZFS) from Ni^{II} and/or antiferromagnetic intermolecular interactions. For complex **2**, predominant ferromagnetic exchange interactions are also evident as χT increases to $89.0 \text{ cm}^3 \text{ mol}^{-1} \text{ K}$ at 4 K, before decreasing to $79.7 \text{ cm}^3 \text{ mol}^{-1} \text{ K}$. For complex **1** $M/N\beta$ at 2 K and 7 Tesla = 26.2 (see Fig. 7 inset), consistent with a high-spin ground state $S = 13$. The magnetization vs. field plots for complex **2** are shown in Fig. S6a in the electronic supporting information where $M/N\beta = 20.9$ at 2 K and 7 Tesla.

To determine the magnitude of the exchange interactions between metal ions in complex **1**, the susceptibility and magnetisation data were fitted simultaneously using the program PHI 2.0.⁶¹ The obtained J values are reported according to the form of the Hamiltonian shown below (eq. 3), to enable comparison to those obtained from the theoretical studies:

$$\begin{aligned} \hat{H} = & -J_1 (\hat{S}_1\hat{S}_7 + \hat{S}_2\hat{S}_8 + \hat{S}_3\hat{S}_7 + \hat{S}_3\hat{S}_8 + \hat{S}_4\hat{S}_7 + \hat{S}_4\hat{S}_8 + \hat{S}_5\hat{S}_7 + \hat{S}_6\hat{S}_8) - \\ & J_2 (\hat{S}_1\hat{S}_3 + \hat{S}_2\hat{S}_3 + \hat{S}_4\hat{S}_5 + \hat{S}_4\hat{S}_6) - J_3 (\hat{S}_3\hat{S}_4) + g_{\text{Ni}}\mu_B\vec{B} \sum_{i=1}^6 \hat{S}_i \\ & + g_{\text{Gd}}\mu_B\vec{B} \sum_{j=7}^8 \hat{S}_j \dots (3) \end{aligned}$$

Note that the large magnetic anisotropy of Dy^{III} precludes a similar fit of the data for **2**. In light of the different bridging angles between the Ni^{II} and Gd^{III} centres in **1**, three different exchange pathways were used in the fit, as shown in Fig. 7. In addition, g -values were fixed to 2.15 for Ni^{II} , 2.0 for Gd^{III} and ZFS was not included, in order to reduce the size and complexity of the computation. The exclusion of ZFS has a more noticeable effect on the fit of the magnetization vs. field data (Fig. 7 inset), as expected for a complex containing Ni^{II}

where ZFS is expected. However, the fit to the χT versus T data is excellent apart from at the very lowest temperatures. The exchange interactions between neighbouring Ni^{II} ions (J_2 and J_3) were found to be $+14.8 (\pm 1.2) \text{ cm}^{-1}$ and $+32.2 (\pm 10.0) \text{ cm}^{-1}$, respectively and the exchange interactions between Ni^{II} and Gd^{III} were found to be $+0.33 (\pm 0.02) \text{ cm}^{-1}$ (J_1). Weak exchange interactions are commonly observed in large Ni^{II} - Gd^{III} complexes and the magnitude of the Ni^{II} - Gd^{III} exchange interactions in **1** agree with those found previously in the literature.^{62–65}

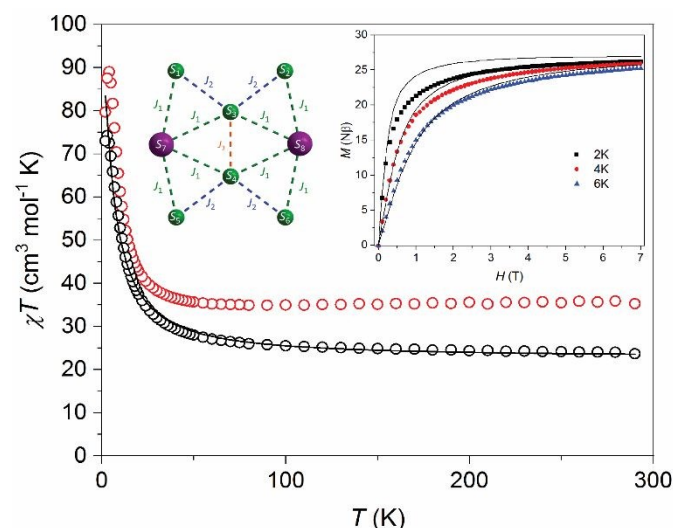


Fig. 7 Temperature dependence of χT for complexes **1** (black open circles) and **2** (red open circles). Inset shows the magnetization vs. field data for complex **1** at 2, 4 and 6 K. The solid black lines correspond to a simultaneous fit of the susceptibility and magnetization data for **1** using the model shown and neglecting zero-field splitting.

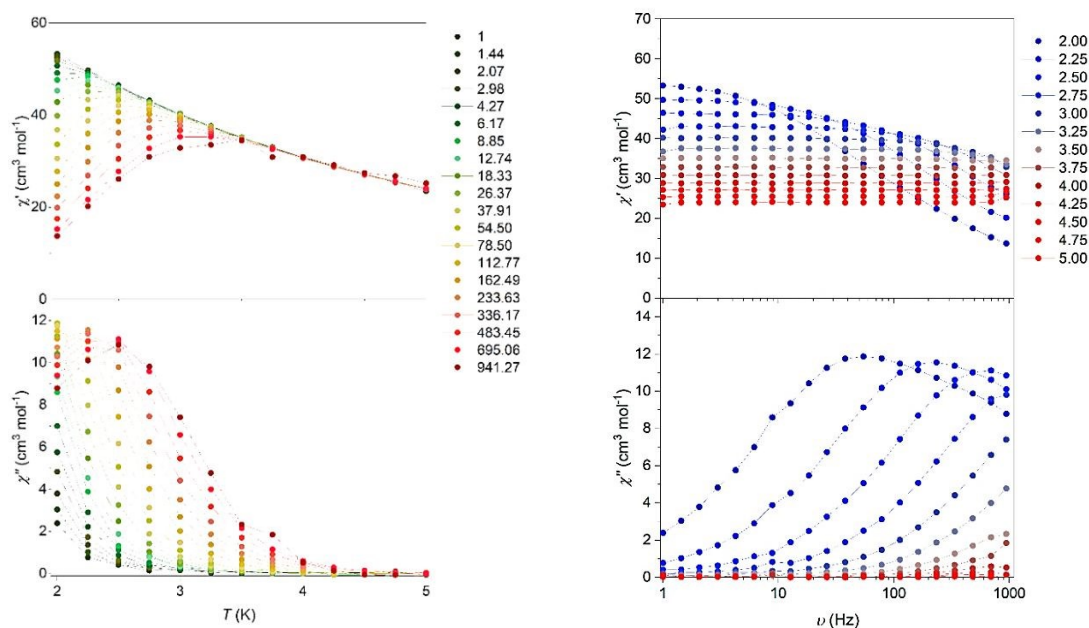


Fig. 8 Left: The in-phase (χ') and out-of-phase (χ'') susceptibility data for complex **2** in a 600 Oe dc applied field. Right: The in-phase (χ') and out-of-phase (χ'') susceptibility data vs. frequency for complex **2** in a 600 Oe dc applied field.

Complex **1** displays no slow magnetic relaxation with, or without, an applied dc field. Complex **2** requires an applied dc field to observe any significant slow magnetic relaxation, consistent with the presence of transverse magnetic anisotropy, which given the structure of **2** could arise from the Ni^{II} and/or Dy^{III} centres. The ac magnetic susceptibility measurements of complex **2** were measured from 1–941 Hz with an optimum applied dc field of 600 Oe (see Fig. S6b). The ac data were then fitted using the program CCFit, in order to derive the relaxation times τ . The in-phase (χ') and out-of-phase (χ'') ac susceptibility vs. temperature data are shown in Fig. 8 and indicate slow relaxation of the magnetization typical of a single-molecule magnet. The Arrhenius plot derived from the data for **2** at 600 Oe is shown in Fig. S7, yielding the energy barrier $U_{\text{eff}} = 19.3$ (0.1) K and the pre-exponential factor $\tau_0 = 1.22$ (0.07) $\times 10^{-7}$ s.

Theoretical Studies

The interpretation of the magnetic properties of **1** and **2** was also supported by theoretical calculations. First, the DFT calculations were used for the estimation of the magnetic exchange coupling within the formalism of the spin Hamiltonian. We used two hybrid functionals B3LYP and PBE0, which recently showed good results for polynuclear systems.^{66–67} In order to facilitate such calculations in complex systems like herein presented complexes **1** and **2**, the broken-symmetry approach was applied in such way that only two paramagnetic ions were preserved in the respective molecular structures extracted from X-ray data, while all other metal atoms were replaced by their diamagnetic analogues (Dy→Lu, Gd→Lu, Ni→Zn). Then, the energy of the broken-symmetry spin state (BS) was compared to the energy of high-spin state (HS), $\Delta = \epsilon_{\text{BS}} - \epsilon_{\text{HS}}$, leading to the isotropic exchange parameter J computed according to the Yamaguchi method^{68–69} as

$$J = 2\Delta / [\langle S^2 \rangle_{\text{HS}} - \langle S^2 \rangle_{\text{BS}}] \dots (4)$$

for spin Hamiltonian of the form

$$\hat{H} = -J(\vec{S}_1 \cdot \vec{S}_2) \dots (5)$$

The respective results together with selected structural parameters are listed in Table 1 and the calculated spin density plots for selected cases are shown in Fig. S8 in the electronic supporting information. As there are various types and combinations of the bridging ligands (OH, H₂O, OPh, Cl) it is hard to deduce magneto-structural correlation (Fig. 9). However, it is evident that at least for Ni–(μ -OH)₂–Ni bridge, the decreasing the Ni–Ni distance and/or average Ni–O–Ni angle led to switching of antiferromagnetic to ferromagnetic exchange interaction as expected from the other studies of similar systems.^{70–72} The validity of these calculations was assessed by the comparison of calculated magnetic properties using DFT-derived J -values with the experimental data (Fig. 10). Evidently, both functionals correctly predict the increase of χT product due to prevailing ferromagnetic exchange interactions, however, only PBE0 functional correctly predicted $S = 13$ ground state as visualized in plots of the spin energy levels in Fig. S10 in the ESI, and therefore excellent agreement with the experimental magnetic data was achieved. Moreover, the magnetic anisotropy of Ni^{II} was also evaluated by CASSCF method (Table 2, *vide infra*), but the large dimension of interaction matrices, $3^6 8^2 = 46656$, makes the direct computation of magnetic properties of **1** with ZFS impossible. In the case of compound **2**, both DFT functional supported large ferromagnetic Ni–Ni exchange coupling in accordance with the experimental data showing an increase of χT on cooling. However, the ground state $^6\text{H}_{15/2}$ of Dy^{III} ion cannot be described by the spin Hamilton formalism, and therefore the computation of Ni–Dy magnetic interactions is precluded by DFT. However, the post-Hartree–Fock CASSCF calculations were utilized in order to better understand the magnetic properties of these compounds. Thus, the CASSCF calculations were performed with OpenMOLCAS program for Ni^{II} ions of **1** and **2** and also for Dy^{III} ion for **2** by leaving only one Ni or Dy atom in molecular structures and replacing all other paramagnetic ions by Zn or Lu atoms. The spin-orbit coupling affecting ligand field multiplets of $^6\text{H}_{15/2}$ atomic term were subsequently analysed with the SINGLE_ANISO module of OpenMOLCAS and the relevant parameters of all eight Kramers doublets are listed in Table 3. Ground states of Dy^{III} ion in **2** has a very large axial magnetic anisotropy, $g_x = g_y \approx 0$

Table 1. The DFT calculated J -parameters for Gd–Ni and Ni–Ni pairs in **1** and **2**

M–M' pairs	d(M–M') (Å)	$\angle(\text{M–X–M}')_{\text{av}}$ (°)	J (cm ^{−1}) B3LYP	J (cm ^{−1}) PBE0	J (cm ^{−1}) fitted	Bridging ligands	Compound
Gd1Ni1	3.476	104.145	1.38	1.43	+0.33(±0.02)	OH, OPh	1
Gd1Ni2	3.470	103.61	1.15	1.24	+0.33(±0.02)	OH, OPh	1
Gd1Ni3	3.453	102.47	0.92	0.91	+0.33(±0.02)	OH, OH	1
Gd1Ni3'	3.471	102.79	0.44	0.52	+0.33(±0.02)	OH, OH	1
Ni1Ni3	3.164	97.305	9.70	9.03	+14.8 (±1.2)	H ₂ O, OH	1
Ni2Ni3	3.122	96.3	−4.86	−0.78	+14.8 (±1.2)	OH, OH	1
Ni3Ni3'	2.982	92.87	21.2	17.3	32.2(±10.0)	OH, OH	1
Ni1Ni2	3.079	97.025	30.4	26.1		OH, OPh	2
Ni2Ni3	3.110	89.63	22.7	19.4		Cl, OPh	2

and $g_z \approx 19.1$, and first and second excited states separated by 131 and 205 cm^{-1} also possess large axial magnetic anisotropy (Table 3). The orientation of g_z -axes of these three states is visualized in Fig. 11 and they are oriented almost in the same direction, which may generally improve the SMM properties. Next, the plot of the magnetization blocking barrier was constructed (Fig. 11), where the values of the transition magnetic moments between Kramers levels are shown and this plot suggests that there is a very low probability of the quantum tunneling of the ground state, but temperature-assisted quantum tunneling is possible through the first and second excited states and there is very high probability of magnetization reversal through the third excited state. Similarly, SINGLE_ANISO module applied to CASSCF calculation of Ni atoms resulted in single-ion zero-field splitting parameters D and E , and g -factors listed in Table 2.

The calculated D -values are in the range $-19\text{ cm}^{-1} < D < 20\text{ cm}^{-1}$, thus rather large values were achieved for octahedrally coordinated Ni^{II} ions in **1** and **2**, because ideal O_h symmetry of the ligand field would result in zero value of D .⁷³ This can be explained by deviation from O_h symmetry (Table S2) and also by heteroleptic coordination sphere. However, the extremely large value of $D = -194\text{ cm}^{-1}$ was found for tetra-coordinate Ni3 atom of **2**, which may significantly contribute to the overall magnetic anisotropy of **2**. The ideal T_d symmetry of the ligand field would result in 3T_1 ground state, however, the *Jahn-Teller* effect induced deformation of $\{\text{NiCl}_3\text{O}\}$ chromophore, but the contribution of the low-lying excited states to ZFS parameters is still enormous. The respective energies of ligand field terms and multiplets are showed in Fig. S11. Usually, NEVPT2 or CASPT2 additional correction are needed to better predict ZFS parameters of 3d-metals, which is prohibited here by large number of atoms in **2**. Nevertheless, the small molecular fragment was extracted for which we were able to perform CASSCF/CASPT2 calculations clearly confirming very large D parameter of Ni3 atom in **2** (Fig. S12, ESI).

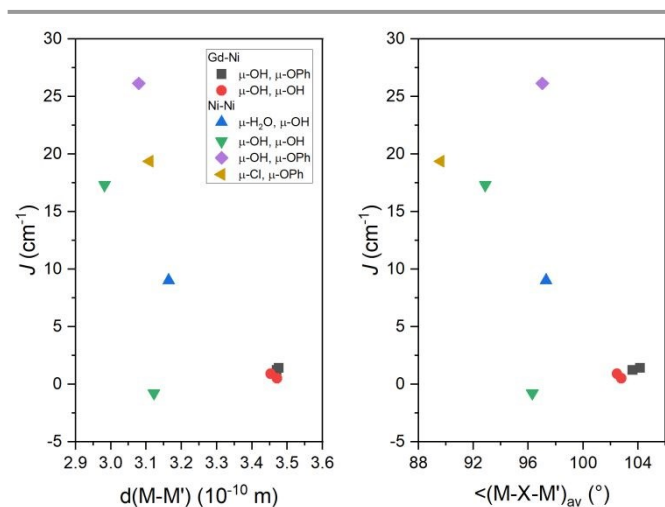


Fig. 9 The variation of J-parameters calculated by PBE0 functional for compounds **1** and **2** for various bridging modes.

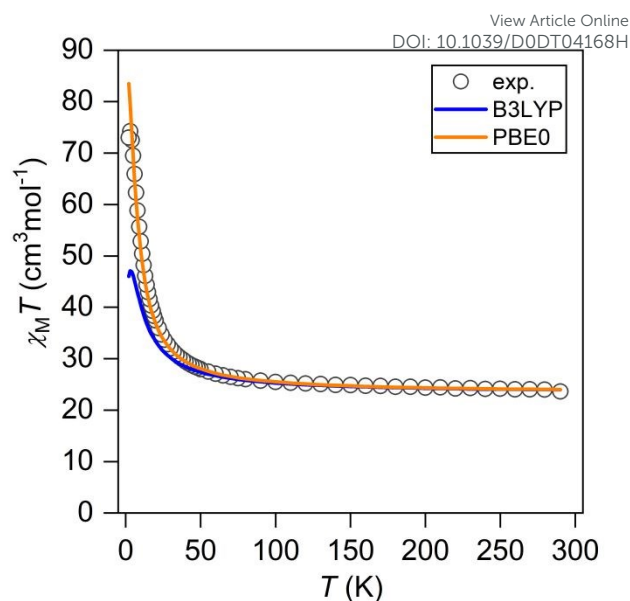


Fig. 10 The calculation of magnetic properties of **1** based on *J*-parameters in Table 1 and average *g*-value equal 2.07. Experimental data are plotted as empty circles and the calculated data are showed as blue line for B3LYP's derived *J*-parameters and as orange line for PBE0's derived *J*-parameters.

So far, such large D -parameters were usually reported for penta-coordinate Ni^{II} complexes approaching D_{3h} symmetry with $D = -400$ to -535 cm^{-1} ,⁷⁴ $D = -185 \text{ cm}^{-1}$,⁷⁵ while quite large $D = 45.4 \text{ cm}^{-1}$ was found for tetrahedral complex with $\{\text{NiSe}_4\}$ chromophore.⁷⁶ Next the POLY_ANISO module was applied to analyse the dipole-dipole interaction of the ground states magnetic moments of two Dy^{III} ions of **2**, which are interconnected by the inversion operation of the symmetry. The orientation of the magnetic moment with respect to $\text{Dy}\cdots\text{Dy}$ linking line (angle θ) in such centro-symmetric compounds is the crucial factor for the nature of the dipole-dipole interaction, either antiferromagnetic or ferromagnetic, due to the following relationship for the energy of the dipole-dipole interaction.⁷⁷

$$E_{\text{dipolar}} = -\frac{\mu_0}{4\pi} \frac{\mu_i \mu_j}{r^3} (3 \cos^2 \theta - 1) \quad \dots(6)$$

Therefore, the ferromagnetic interaction is expected for $\theta < 54.7^\circ$, whereas for $\theta > 54.7^\circ$ the antiferromagnetic interaction is predicted. In the case of compound **2**, the angle θ equals 84° and therefore the antiferromagnetic dipolar interaction is expected. Indeed, POLY_ANISO calculations between two ground state Kramers doublets of both Dy atoms confirmed such expectation as is depicted in Fig. S11 in the ESI. Thus, this interaction may be responsible for speeding up the relaxation of the magnetization. However, we are aware that the exchange coupling of the types Dy...Dy and Dy...Ni may also contribute to the whole picture of the magnetization blocking barrier significantly leading to further modification of dynamic magnetic properties of **2**. Therefore, the experimental magnetic susceptibility of **2** was fitted with a home-made

Table 2. CASSCF/DKH2/SINGLE_ANISO calculated parameters for Ni atoms in **1** and **2**

	$D \text{ (cm}^{-1}\text{)}$	$E \text{ (cm}^{-1}\text{)}$	E/D	$g\text{-factors } (g_x, g_y, g_z)$
Ni1 of 1	-18.7	5.35	-0.287	2.239, 2.323, 2.411
Ni2 of 1	10.4	-2.87	-0.275	2.340, 2.303, 2.245
Ni3 of 1	-8.44	2.31	-0.274	2.295, 2.331, 2.374
Ni1 of 2	-9.39	1.97	-0.210	2.256, 2.288, 2.342
Ni2 of 2	19.9	-5.37	-0.271	2.415, 2.348, 2.235
Ni3 of 2	-194	21.0	-0.108	2.310, 2.401, 3.558

Table 3. CASSCF/DKH2/SINGLE_ANISO calculated energy levels for the complex $[\text{Zn}_6\text{DyLu}]$ of **2** with the respective g -factors for each Kramers doublet with effective spin $\frac{1}{2}$

$E \text{ (cm}^{-1}\text{)}$	g_x	g_y	g_z
0.0	0.002	0.005	19.116
130.6	0.149	0.273	14.537
205.1	0.045	0.347	12.277
324.0	2.646	3.563	9.452
423.8	3.080	5.187	8.534
508.7	1.781	3.620	11.682
561.6	2.138	3.607	14.214
651.5	0.334	0.616	17.849

The wave-function for the ground state is dominated by $86\%|\pm 15/2\rangle + 13\%|\pm 11/2\rangle$, while the first excited state is dominated by $54\%|\pm 13/2\rangle + 42\%|\pm 9/2\rangle$ and the second excited state is dominated by $49\%|\pm 7/2\rangle + 38\%|\pm 11/2\rangle + 8\%|\pm 15/2\rangle$

routine in cooperation with POLY_ANISO module. According to the molecular structure of **2**, six different magnetic exchange coupling can be expected between nearest-neighbour paramagnetic Dy or Ni atoms. Such a large number of free parameters would lead to over-parameterization of the model, thus J -values of Ni...Ni interactions were set to values calculated by DFT calculation with PBE0 functional. Moreover, Dy1...Ni1, Dy1...Ni2* and Dy1...Ni1* were expected to be equal having similar Dy...Ni distances. Therefore, we are left with just two free parameters, namely $J_{\text{Dy-Dy}}$ and $J_{\text{Dy-Ni}}$ interactions.

Furthermore, the calculations were limited to the inclusion of two lowest Kramers doublets resulting in already $3^{642} = 11664$ states that needed to be calculated by POLY_ANISO for each fitting iteration. A reasonably good fit was achieved with

$J_{\text{Dy-Dy}} = -0.39 \text{ cm}^{-1}$ and $J_{\text{Dy-Ni}} = 2.02 \text{ cm}^{-1}$, which means the antiferromagnetic exchange between dysprosium ions and the ferromagnetic exchange between nickel and dysprosium ions – Fig. 12. The plot of local D -tensor axes of Ni atoms and local g -tensor of Dy atoms together with the orientation of the molecular g -tensor of the ground state doublet is shown in Fig. S14. Next, having at disposal information about all single-ion anisotropies and magnetic exchange parameters, the magnetization reversal barrier plot was made for **2** taking into account 20 lowest Kramers doublet states as depicted in Fig. 12. The barrier can be crossed through states located at $\sim 10 \text{ cm}^{-1}$ which agrees well with energy barrier $U_{\text{eff}} = 19.3 \text{ K}$ derived by AC susceptibility data. However, the herein presented theoretical analysis found a diminishing probability of quantum tunneling of magnetization through the ground state, which suggests that **2** should be zero-field SMM, which contradicts the experiment. The most probable explanation of these conflicts can be explained by intermolecular interactions in the solid-state which also contribute to the tunneling mechanism.

Conclusions

Coordination driven hydrolysis reaction triggered the hetero-metallic aggregation potency of L^{2-} for cooperative binding of Ni^{II} and $\text{Gd}^{\text{III}}/\text{Dy}^{\text{III}}$ metal ions. Selective coordination of Ni^{II} and $4f$ ions by multiple number of ligand anions have established hydroxido, chlorido and aqua bridge-driven aggregation reactions for the generation of two different types of 3d-4f coordination aggregates. During the formation of complex **1**, entrapment of in-situ formed $\text{Ni}_2(\text{OH})_2$ unit and for **2**, the terminal NiCl_2 unit, supports the formation of both the molecular architecture. The solution chemistry of Gd^{III} and Dy^{III} ions in the MeOH-CHCl_3 medium are different in terms of liquid-liquid equilibrium, in situ formed reactive species and Lewis acidity of the $4f$ metal ions. Thus, the interchange of the $4f$ ions (Gd^{III} vs. Dy^{III}) has substantial consequences in the

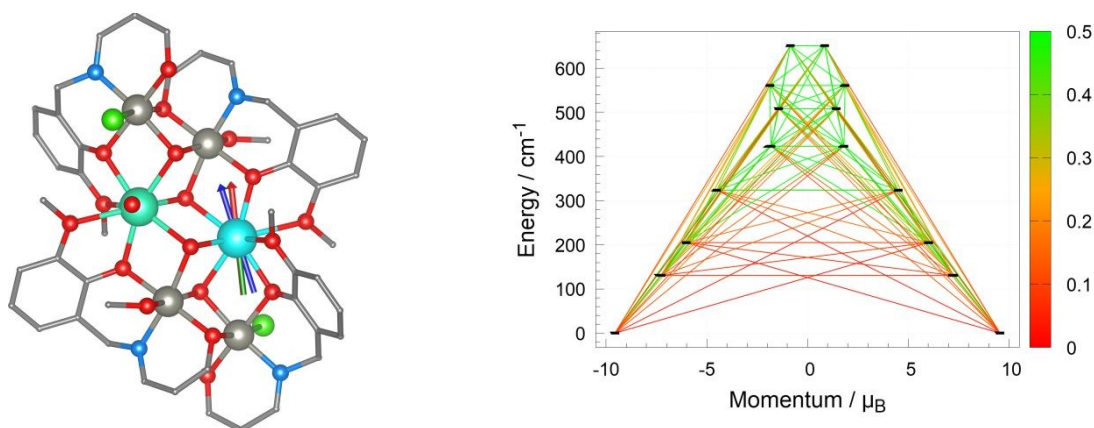


Fig. 11 Left: ab initio computed orientation of the principal magnetization axis (g_z) of the ground-state (red arrow) and first two excited states (green and blue arrows) in $[\text{Zn}_6\text{DyLu}]$ of **2**. Right: Magnetization blocking barrier of Dy^{III} in **2**, where magnetic relaxation path, outlining the blocking barrier, is traced by the red-green lines scaling the transition magnetic dipole matrix elements between the connected multiplet states.

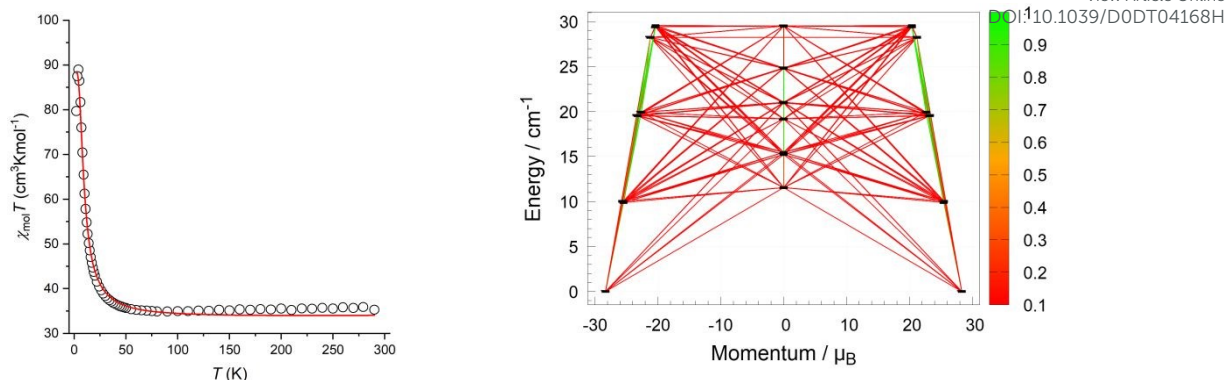


Fig. 12 Left: the fit of experimental magnetic susceptibility of **2** with $J_{\text{Dy-Dy}} = -0.39 \text{ cm}^{-1}$, $J_{\text{Dy-Ni}} = 2.02 \text{ cm}^{-1}$, $J_{\text{Ni1-Ni2}} = 26.14 \text{ cm}^{-1}$, $J_{\text{Ni2-Ni3}} = 19.38 \text{ cm}^{-1}$ calculated with POLY_ANISO using scaling coefficient 0.86. Right: Magnetization blocking barrier of complex **2**, where magnetic relaxation path, outlining the blocking barrier, is traced by the red-green lines scaling the transition magnetic dipole matrix elements between the connected multiplet states.

serendipitous yet standardized new synthesis and structural aspects, discovering mineralization like coordination aggregation pathways. The resulting 3d-4f metal ion-based core structure and the topology of **1** and **2**, led to predominantly ferromagnetic exchange coupling interactions with large magnetic ground states as proofed by DC magnetic data as well as by DFT calculations. The antiferromagnetic exchange and dipolar interaction between Dy^{III} ions were established by analysis of the respective CASSCF calculations with SINGLE_ANISO and POLY_ANISO modules in respect to the experimental data, revealing ferromagnetic exchange between Ni^{II} and Dy^{III} ions. The scheme of the magnetic moment reversal barrier was provided for **2** helping us to rationalize the experimentally found U_{eff} value 19.3 K, while the necessity to apply small static magnetic field to suppress the quantum tunneling of the magnetization was ascribed to the intermolecular interactions in solid state.

Conflicts of interest

The authors declare no conflict of interest.

Acknowledgements

A.B. is thankful to DST-INSPIRE for the research fellowship. We acknowledge FIST program of DST, New Delhi for the Single Crystal XRD facility at the Department of Chemistry, IIT Kharagpur. M.M. thanks the University of Glasgow for financial support. R.H. acknowledges the financial support from the institutional sources of the Department of Inorganic Chemistry, Palacký University Olomouc, Czech Republic.

References

- 1 D. N. Woodruff, R. E. P. Winpenny and R. A. Layfield, *Chem. Rev.*, 2013, **113**, 5110–5148.
- 2 G. Christou, D. Gatteschi, D. N. Hendrickson and R. Sessoli, *MRS Bull.*, 2000, **25**, 66–71.
- 3 M. Affronte, *J. Mater. Chem.*, 2009, **19**, 1731–1737.
- 4 M. N. Leuenberger, D. Loss, *Nature*, 2001, **410**, 789–793.
- 5 P. C. E. Stamp and A. Gaita-Arino, *J. Mater. Chem.*, 2009, **19**, 1718–1730.
- 6 L. Bogani and W. Wernsdorfer, *Nature Materials*, 2008, **7**, 179–186.
- 7 W. Wernsdorfer, *Int. J. Nanotechnol.*, 2010, **7**, 497–522.
- 8 E. Ruiz, J. Cirera, J. Cano, S. Alvarez, C. Loose and J. Kortus, *Chem. Commun.*, 2008, 52–54.
- 9 F. Neese and D. A. Pantazis, *Faraday Discuss.*, 2011, **148**, 229–238.
- 10 Y. Li, Q. Shang, Y.-Q. Zhang, E.-C. Yang and X.-J. Zhao, *Chem. Eur. J.*, 2016, **22**, 18840–18849.
- 11 W. Wernsdorfer, N. Aliaga-Alcalde, D. N. Hendrickson and G. Christou, *Nature*, 2002, **416**, 406–409.
- 12 S. Osa, T. Kido, N. Matsumoto, N. Re, A. Pochaba and J. A. Mrozinski, *J. Am. Chem. Soc.*, 2004, **126**, 420–421.
- 13 S. K. Singh, T. Gupta, P. Badkur and G. Rajaraman, *Chem. Eur. J.*, 2014, **20**, 10305–10313.
- 14 E. Moreno-Pineda, N. F. Chilton, F. Tuna, R. E. P. Winpenny and E. J. L. McInnes, *Inorg. Chem.*, 2015, **54**, 5930–5941.
- 15 K. C. Mondal, G. E. Kostakis, Y. Lan, W. Wernsdorfer, C. E. Anson and A. K. Powell, *Inorg. Chem.*, 2011, **50**, 11604–11611.
- 16 N. Ahmed, C. Das, S. Vaidya, S. K. Langley, K. S. Murray and M. Shanmugam, *Chem. Eur. J.*, 2014, **20**, 14235–14239.
- 17 A. Bhanja, R. Herchel, Z. Travníček and D. Ray, *Inorg. Chem.*, 2019, **58**, 12184–12198.
- 18 H. Wu, M. Li, S. Zhang, H. Ke, Y. Zhang, G. Zhuang, W. Wang, Q. Wei, G. Xie and S. Chen, *Inorg. Chem.*, 2017, **56**, 11387–11397.
- 19 Z. Zhang, Y. Zhang and Z. Zheng, *Struct. Bond.*, 2017, **173**, 1–49.
- 20 R. Wang, H. Liu, M. D. Carducci, T. Jin, C. Zheng and Z. Zheng, *Inorg. Chem.*, 2001, **40**, 2743–2750.
- 21 C. Papatriantafyllopoulou, T. C. Stamatatos, C. G. Efthymiou, L. Cunha-Silva, F. A. A. Paz, S. P. Perlepes and G. Christou, *Inorg. Chem.*, 2010, **49**, 9743–9745.
- 22 J.-B. Peng, Q.-C. Zhang, X.-J. Kong, Y.-P. Ren, L.-S. Long, R.-B. Huang, L.-S. Zheng and Z. Zheng, *Angew. Chem. Int. Ed.*, 2011, **50**, 10649–10652.
- 23 Z.-M. Zhang, L.-Y. Pan, W.-Q. Lin, J.-D. Leng, F.-S. Guo, Y.-C. Chen, J.-L. Liu and M.-L. Tong, *Chem. Commun.*, 2013, **49**, 8081–8083.
- 24 J.-J. Zhang, T.-L. Sheng, S.-Q. Xia, G. Leibel, F. Meyer, S.-M. Hu, R.-B. Fu, S.-C. Xiang and X.-T. Wu, *Inorg. Chem.*, 2004, **43**, 5472–5478.
- 25 A. Bhanja, E. Moreno-Pineda, R. Herchel, W. Wernsdorfer and D. Ray, *Dalton Trans.*, 2020, **49**, 7968–7976.

- 26 B. S. Furniss, A. J. Hannaford, P. W. G. Smith and A. R. Tatchell, *Vogel's Text book of Practical Organic Chemistry*, 5th ed.; ELBS, Longman: London, U.K. 1989.
- 27 I. Zagol-Ikapitte, V. Amarnath, M. Bala, L. J. Roberts, J. A. Oates and O. Boutaud, *Chem. Res. Toxicol.*, 2010, **23**, 240–250.
- 28 A. Bhanja, M. Schulze, R. Herchel, E. Moreno-Pineda, W. Wernsdorfer and Debashis Ray, *Inorg. Chem.*, 2020, in press, doi: 10.1021/acs.inorgchem.0c02148.
- 29 SAINT, SMART and XPREP, Siemens Analytical X-ray Instruments Inc., Madison, WI, 1995.
- 30 G. M. Sheldrick, *SHELXS-2014*, Program for Crystal Structure Solution, University of Göttingen, 2014.
- 31 G. M. Sheldrick, *Acta Crystallogr. Sect. A: Found. Crystallogr.*, 2008, **64**, 112–122.
- 32 O. V. Dolomanov, L. J. Bourhis, R. J. Gildea, J. A. K. Howard, H. J. Puschmann, *Appl. Cryst.*, 2009, **42**, 339–341.
- 33 G. M. Sheldrick, SADABS Software for Empirical Absorption Correction, University of Göttingen, Institute für Anorganische Chemie der Universität, Göttingen, Germany, 1999–2003.
- 34 DIAMOND, Visual Crystal Structure Information System, version 3.1, Crystal Impact: Bonn, Germany, 2004.
- 35 F. Neese, *Wiley Interdiscip. Rev. Comput. Mol. Sci.*, 2012, **2**, 73–78.
- 36 F. Neese, *Wiley Interdiscip. Rev. Comput. Mol. Sci.*, 2018, **8**, e1327.
- 37 C. Lee, W. Yang and R. G. Parr, *Phys. Rev. B: Condens. Matter Mater. Phys.*, 1988, **37**, 785–789.
- 38 A. D. J. Becke, *Chem. Phys.*, 1993, **98**, 1372–1377.
- 39 A. D. J. Becke, *Chem. Phys.*, 1993, **98**, 5648–5652.
- 40 P. J. Stephens, F. J. Devlin, C. F. Chabalowski and M. J. J. Frisch, *Phys. Chem.*, 1994, **98**, 11623–11627.
- 41 M. Douglas and N. M. Kroll, *Ann. Phys. (N. Y.)*, 1974, **82**, 89–155.
- 42 B. A. Hess, *Phys. Rev. A*, 1986, **33**, 3742–3748.
- 43 D. Aravena, F. Neese and D. A. Pantazis, *J. Chem. Theory Comput.*, 2016, **12**, 1148–1156.
- 44 F. Weigend and R. Ahlrichs, *Phys. Chem. Chem. Phys.*, 2005, **7**, 3297–3305.
- 45 L. Visscher and K. G. Dyall, *Atom. Data Nucl. Data Tables.*, 1997, **67**, 207–224.
- 46 F. Neese, F. Wennmohs, A. Hansen and U. Becker, *Chem. Phys.*, 2009, **356**, 98–109.
- 47 R. Izsák and F. Neese, *J. Chem. Phys.*, 2011, **135**, 144105.
- 48 B. O. Roos, *Adv. Chem. Phys.*, 1987, **69**, 399–445.
- 49 I. F. Galván, M. Vacher, A. Alavi, C. Angeli, F. Aquilante, J. Autschbach, J. J. Bao, S. I. Bokarev, N. A. Bogdanov, R. K. Carlson, L. F. Chibotaru, J. Creutzberg, N. Dattani, M. G. Delcey, S. S. Dong, A. Dreuw, L. Freitag, L. M. Frutos, L. Gagliardi, F. Gendron, A. Giussani, L. González, G. Grell, M. Guo, C. E. Hoyer, M. Johansson, S. Keller, S. Knecht, G. Kovačević, E. Källman, G. L. Manni, M. Lundberg, Y. Ma, S. Mai, J. P. Malhado, P. Å. Malmqvist, P. Marquetand, S. A. Mewes, J. Norell, M. Olivucci, M. Oppel, Q. M. Phung, K. Pierloot, F. Plasser, M. Reiher, A. M. Sand, I. Schapiro, P. Sharma, C. J. Stein, L. K. Sørensen, D. G. Truhlar, M. Ugandi, L. Ungur, A. Valentini, S. Vancoillie, V. Veryazov, O. Weser, T. A. Wesolowski, P.-O. Widmark, S. Wouters, A. Zech, J. P. Zobel and R. Lindh, *J. Chem. Theory Comput.*, 2019, **15**, 5925–5964.
- 50 B. A. Heß, C. M. Marian, U. Wahlgren and O. Gropen, *Chem. Phys. Lett.*, 1996, **251**, 365–371.
- 51 B. Schimmelpfennig. AMFI, an atomic mean-field spin-orbit integral program. Stockholm University, 1996.
- 52 B. O. Roos, R. Lindh, P.-Å. Malmqvist, V. Veryazov, P.-O. Widmark and A. C. Borin, *J. Phys. Chem. A*, 2008, **112**, 11431–11435.
- 53 B. O. Roos, R. Lindh, P.-Å. Malmqvist, V. Veryazov and P.-O. Widmark, *Chem. Phys. Lett.*, 2005, **409**, 295–299.
- 54 L. F. Chibotaru, L. Ungur and A. Soncini, *Angew. Chemie Int. Ed.*, 2008, **47**, 4126–4129.
- 55 L. F. Chibotaru and L. Ungur, *J. Chem. Phys.*, 2012, **137**, 064112.
- 56 L. Ungur, M. Thewissen, J.-P. Costes, W. Wernsdorfer and L. F. Chibotaru, *Inorg. Chem.*, 2013, **52**, 6328–6337.
- 57 C. F. Macrae, I. Sovago, S. J. Cottrell, P. T. A. Galek, P. McCabe, E. Pidcock, M. Platings, G. P. Shields, J. S. Stevens, M. Towler and P. A. Wood, *J. Appl. Cryst.*, 2020, **53**, 226–235.
- 58 K. Momma and F. Izumi, *J. Appl. Crystallogr.*, 2011, **44**, 1272–1276.
- 59 J.-P. Costes, F. Dahan, L. Vendier, S. Shova, G. Lorusso, M. Evangelisti, *Dalton Trans.*, 2018, **47**, 1106–1116.
- 60 L. Yang, D. R. Powell and R. P. Houser, *Dalton Trans.*, 2007, 955–964.
- 61 N. F. Chilton, R. P. Anderson, L. D. Turner, A. Soncini and K. S. Murray, *Comput. Chem.*, 2013, **34**, 1164–1175.
- 62 A. B. Canaj, D. I. Tzimopoulos, M. Siczek, T. Lis, R. Inglis and C. J. Milios, *Inorg. Chem.*, 2015, **54**, 7089–7095.
- 63 S. Wang, X. Yang, J. Qian, Q. Li, Z. Chen, L. Zhang, S. Huang, C. Wang and R. A. Jones, *Dalton Trans.*, 2017, **46**, 1748–1752.
- 64 G.-J. Zhou, W.-P. Chen, Y. Yu, L. Qin, T. Han and Y.-Z. Zheng, *Inorg. Chem.*, 2017, **56**, 12821–12829.
- 65 T. N. Hooper, J. Schnack, S. Piligkos, M. Evangelisti and E. K. Brechin, *Angew. Chem. Int. Ed.*, 2012, **51**, 4633–4636.
- 66 M. Machata, I. Nemec, R. Herchel and Z. Trávníček, *RSC Adv.*, 2017, **7**, 25821–25827.
- 67 R. Herchel, I. Nemec, M. Machata and Z. Trávníček, *Inorg. Chem.*, 2015, **54**, 8625–8638.
- 68 K. Yamaguchi, Y. Takahara and T. Fueno, V.H. Smith (Ed.) *Applied Quantum Chemistry*. Reidel, Dordrecht. 1986, pp 155.
- 69 T. Soda, Y. Kitagawa, T. Onishi, Y. Takano, Y. Shigeta, H. Nagao, Y. Yoshioka and K. Yamaguchi, *Chem. Phys. Lett.*, 2000, **319**, 223–230.
- 70 R. Herchel, I. Nemec, M. Machata and Z. Trávníček, *Dalton Trans.*, 2016, **45**, 18622–18634.
- 71 M. A. Halcrow, J. Sun, J. C. Huffman and G. Christou, *Inorg. Chem.*, 1995, **34**, 4167–4177.
- 72 A. Das, F. J. Klinker, S. Demeshko, S. Meyer, S. Dechert and F. Meyer, *Inorg. Chem.*, 2012, **51**, 8141–8149.
- 73 R. Boča, *Coord. Chem. Rev.*, 2004, **248**, 757–815.
- 74 K. E. R. Marriott, L. Bhaskaran, C. Wilson, M. Medarde, S. T. Ochsenbein, S. Hill and M. Murrie, *Chem. Sci.*, 2015, **6**, 6823–6828.
- 75 K. A. Schulte, K. R. Vignesh and K. R. Dunbar, *Chem. Sci.*, 2018, **9**, 9018–9026.
- 76 S. D. Jiang, D. Maganas, N. Levesanos, E. Ferentinos, S. Haas, K. Thirunavukkuarasu, J. Krzystek, M. Dressel, L. Bogani, F. Neese and P. Kyritsis, *J. Am. Chem. Soc.*, 2015, **137**, 12923–12928.
- 77 J.-D. Leng, J.-L. Liu, W.-Q. Lin, S. Gómez-Coca, D. Aravena, E. Ruiz and M.-L. Tong, *Chem. Commun.*, 2013, **49**, 9341–9343.